Single-crystelline hexagonal silicon-germanium

Hauge, HIT; Hauge, T; Conesa Boj, Sonia; Verheijen, M.A.; Koelling, S.; Bakkers, Erik

DOI
10.1021/acs.nanolett.6b03488

Publication date
2017

Document Version
Final published version

Published in
Nano Letters: a journal dedicated to nanoscience and nanotechnology

NANO LETTERS

Letter

pubs.acs.org/NanoLett

Single-Crystalline Hexagonal Silicon–Germanium

Håkon Ikaros T. Hauge,[†] Sonia Conesa-Boj,[†,§] Marcel A. Verheijen,[†,‡] Sebastian Koelling,[†] and Erik P. A. M. Bakkers*[,†,§]

[†]Department of Applied Physics, Eindhoven University of Technology, 5600 MB Eindhoven, The Netherlands

[‡]Philips Innovation Laboratories, High Tech Campus 11, 5656 AE Eindhoven, The Netherlands

[§]Kavli Institute of Nanoscience, Delft University of Technology, 2628 CJ Delft, The Netherlands

ABSTRACT: Group IV materials with the hexagonal diamond crystal structure have been predicted to exhibit promising optical and electronic properties. In particular, hexagonal silicon–germanium ($Si_{1-x}Ge_x$) should be characterized by a tunable direct band gap with implications ranging from Si-based light-emitting diodes to lasers and quantum dots for single photon emitters. Here we demonstrate the feasibility of high-quality defect-free and wafer-scale hexagonal $Si_{1-x}Ge_x$ growth with precise control of the alloy composition and layer thickness. This is achieved by transferring the hexagonal phase from a GaP/Si core/shell nanowire template, the same method successfully employed by us to realize hexagonal Si. We determine the optimal growth conditions in order to achieve single-crystalline layer-by-layer $Si_{1-x}Ge_x$ growth in the preferred stoichiometry region. Our results pave the way for exploiting the novel properties of hexagonal $Si_{1-x}Ge_x$ alloys in technological applications.

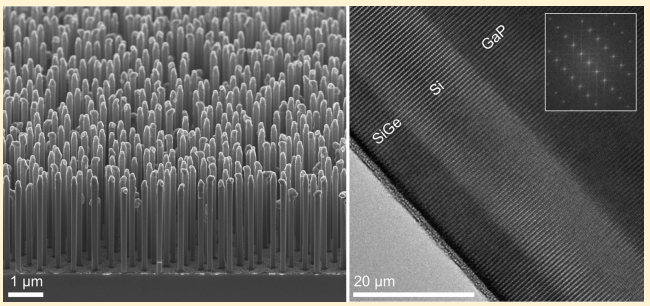

KEYWORDS: *Silicon–germanium, hexagonal crystal structure, core/shell nanowire, single-crystalline, growth rate, kinetics*

Si with the diamond cubic crystal structure is the most widely used technological semiconductor. Unfortunately it lacks in its optical properties because in this crystal phase it exhibits an indirect band gap.[1−3] The integration of an element, displaying efficient interaction with light, with Si technology is of high technological interest. Unfortunately III–V materials that display this behavior have lattice mismatch issues with Si. Ge, a group-IV semiconductor like Si, with the diamond cubic crystal structure also exhibits an indirect band gap. Interestingly, Ge with the hexagonal diamond crystal structure is predicted to present a direct band gap of 0.3 eV, which corresponds to a wavelength of 4.1 μm in the infrared, predicted by the empirical pseudopotential method with spin–orbit interactions.[4] Other studies have also been carried out that use first-principles calculations[2] and empirical pseudopotential method without spin–orbit interactions.[3] By combining hexagonal Si[5−18] and Ge[19,20] to form an alloy with the hexagonal diamond structure, it should be possible to engineer the band structure in such a way that the direct band gap of the $Si_{1-x}Ge_x$ alloy shifts to higher energies.[2−4,21] On the basis of the predicted band structure of hexagonal Si and Ge, $Si_{0.35}Ge_{0.65}$ could present a direct band gap in the region of 1.7 μm, which is close to the telecommunication wavelength of 1.5 μm. In addition, the lattice mismatch between the $Si_{1-x}Ge_x$ alloy for $x < 1$ and a Si substrate is reduced with respect to that between pure Si and pure Ge. In the literature, band gap engineering with $Si_{1-x}Ge_x$ alloys has been explored by calculation of the electronic structure of cubic $Si_{1-x}Ge_x$ alloys[22−25] and specifically growth of a cubic Ge/SiGe core/shell nanowire (NW) system has been published.[26,27]

Here, we present the growth of hexagonal $Si_{1-x}Ge_x$ throughout the whole range of stoichiometries. We utilize a novel combination between III–V and group-IV materials by using wafer-scale arrays of nontapered and single-crystalline hexagonal GaP/Si core/shell NWs as templates[5] and overgrow them with a second epitaxial SiGe shell using metal–organic vapor phase epitaxy (MOVPE). As a result, we obtain GaP/Si/SiGe core/multishell NWs. We expect that the strain stemming from the lattice mismatch between the inner Si and the outer SiGe shell can be accommodated to some extent by the NW geometry, as has been reported for Ge/Si core–shell NWs,[28] thus contributing to achieve high shell Ge content without introducing dislocations. The growth was carried out on nanoimprinted substrates to provide a high number of NWs -on the wafer scale- and consistency. In ref 29, we explored different temperatures and provided details on the growth conditions and kinetics in order to present high quality single-crystalline hexagonal GaP/Si core–shell systems.[5] These acted as a springboard in order to achieve the new growths presented in this work.

In Figure 1a, we present a scanning electron microscopy (SEM) image with an array of about 7 μm long GaP/Si/SiGe core/multishell NWs. The cross-sectional SEM image at a

Received: August 18, 2016
Revised: November 28, 2016
Published: December 21, 2016

DOI: 10.1021/acs.nanolett.6b03488
Nano Lett. 2017, 17, 85−90

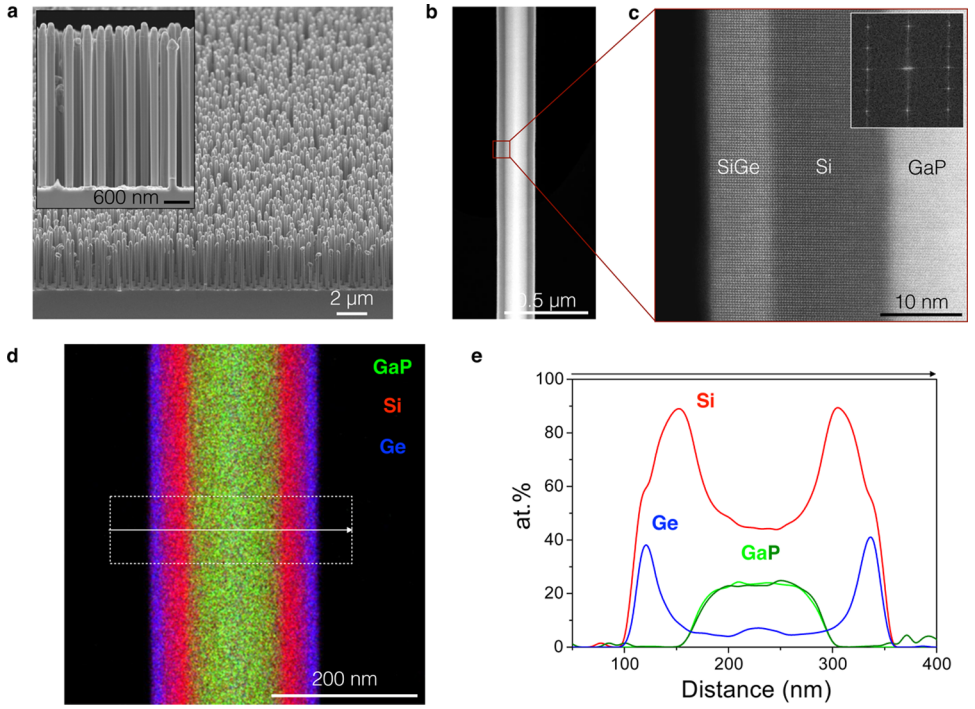

Figure 1. Hexagonal GaP/Si/SiGe core/multishell NWs. (a) SEM image with NW morphology overview of a representative sample (tilt angle 30° normal to substrate). The inset shows a cross-sectional SEM image of the same sample. (b) Low-resolution HAADF STEM image of a representative NW. (c) HAADF HRSTEM image of the SiGe/Si/GaP interfaces viewed in the [11−20] zone axis and the corresponding FFT as inset. (d) EDX map of the NW in (b). The various elements are color-coded to elucidate the structure, green for GaP, red for Si, and blue for Ge. (e) Compositional line profile crossing the structure, averaged over the width of the white dotted rectangle in (d).

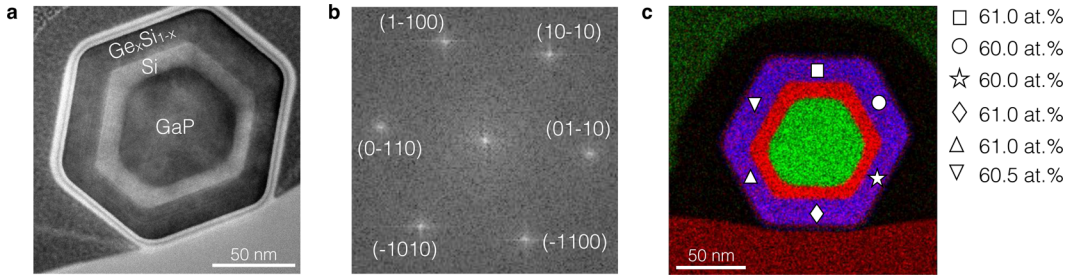

Figure 2. Cross-sectional study of GaP/Si/SiGe core/multishell NWs. (a) Bright-field TEM cross-sectional image of a representative NW. (b) the corresponding FFT to (a). (c) EDX chemical analysis of the same cross-section, where the Ge content in each facet has been averaged and the results in each facet are indicated by different symbols. The color-coding follows the same scheme as in Figure 1d,e.

higher magnification (inset of Figure 1a) shows that the NWs are nontapered with smooth sidewalls. Figure 1b displays a high-angle annular dark-field scanning transmission electron microscopy (HAADF STEM) image of a representative GaP/Si/SiGe core/multishell NW where the SiGe shell has been deposited at 600 °C. The HAADF high-resolution STEM image of the SiGe/Si/GaP interfaces (Figure 1c) viewed in the [11−20] zone axis together with the fast Fourier transform (FFT) (see inset) reveal the hexagonal phase character of the system, as well as the perfect epitaxy between the layers. The composition of the GaP/Si/SiGe core/multishell NWs is confirmed from the energy dispersive X-ray (EDX) spectroscopy map (Figure 1d) and the compositional line profile (Figure 1e) extracted from the map. For this NW, the Ge content measured in terms of atom % is found to be 60.0 ± 0.5 atom % in the outer shell.

To improve our understanding of the vapor−solid shell growth mechanism as well as for future optical characterization experiments it is important to assess the homogeneity of the Ge distribution along the entire shell. We therefore determine the Ge content in the SiGe shell of the samples grown. To quantify the Ge content, the samples were prepared by focused ion beam (FIB) for cross-sectional TEM studies. In Figure 2a, a cross-sectional bright-field (BF) TEM image is shown. The cross-section has been aligned along the [0001] direction. The hexagonal symmetry of the six {1−100} facets of the SiGe shell around the Si shell and GaP core is evident (Figure 2b). The Ge content has been evaluated averaging over positions from each of the six facets, each represented by different symbols in Figure 2c. From this analysis, we indeed find that the Ge content is uniformly distributed in the SiGe shell and in this specific case is around 60.0 ± 0.5 atom %.

To further reveal the SiGe shell growth mechanism, it is useful to plot the resulting incorporated Ge content in the shell, as determined by EDX spectroscopy, as a function of the Ge content in the precursor gas flow in the MOVPE chamber, for all the heterostructures investigated. This is shown in Figure 3a, where we observe a higher incorporation of Ge at the lower

DOI: 10.1021/acs.nanolett.6b03488
Nano Lett. 2017, 17, 85−90

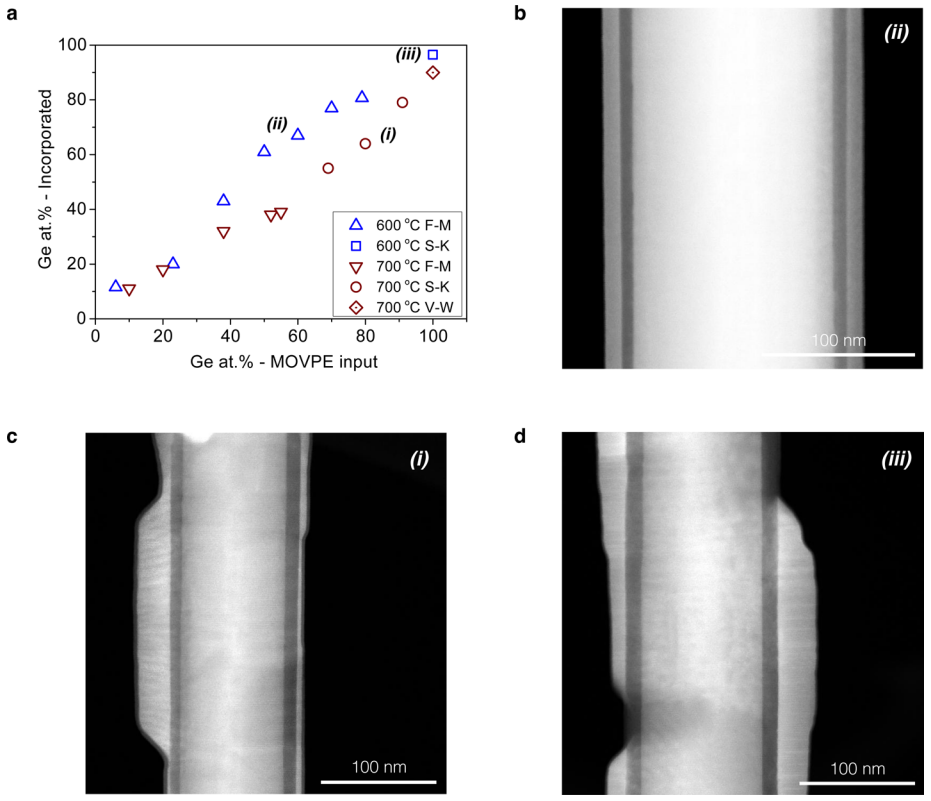

Figure 3. Ge incorporation into the SiGe shell and growth modes. (a) Atom % Ge content incorporated into the SiGe shell, as determined by EDX spectroscopy, as a function of the atom % Ge content in the precursor gas mixture in the MOVPE chamber. (b–d) HAADF STEM image of a sample grown at 600 °C at a Ge content 60 atom % input; 67 atom % incorporated exhibiting F–M growth, 700 °C at 80 atom % input; 66 atom % incorporated exhibiting S–K growth, and 700 °C at 99 atom % input; 91 atom % incorporated exhibiting V–W growth, respectively.

deposition temperature of 600 °C as compared to the one performed at the higher temperature of 700 °C. The fact that the Ge content of the SiGe shell, for the same amount of input Ge (in the vapor phase in the precursor gas mixture) during MOVPE growth, is higher at lower temperatures can be understood as follows. The two precursor gases, namely disilane (Si_2H_6) and germane (GeH_4), have different decomposition temperatures, around 640 °C for Si_2H_6[30] and around 300 °C for GeH_4.[31,32] This means that at 600 °C the Si_2H_6 has not been completely thermally decomposed and therefore the relative amount of Ge available that can be incorporated into the shell is higher. The net result is that at 600 °C the ratio of Ge in the SiGe shell is higher than in the precursor gas mixture. On the other hand, at 700 °C more Si_2H_6 has decomposed, thus more Si is available for deposition and the relative amount of Ge incorporated into the shell decreases.

A characteristic feature of the cubic Si/SiGe system is the appearance of different growth modes as the Ge content; consequently, the lattice strain increases in the SiGe shell[33] and we observe it for the hexagonal phase as well. For most of the samples (for a Ge content of less than 80 atom % grown at 600 °C and of less than 60 atom % grown at 700 °C, indicated by solid symbols in Figure 3a), uniform layers are formed suggesting a Frank–van der Merwe (F–M) layer-by-layer growth mode. Furthermore, all the samples grown at 600 °C up to the Ge content of 80 atom % are defect-free. As can be observed in Figure 3a,c, the samples grown at 700 °C at a Ge content above 60 atom % exhibit a thin SiGe layer combined with the formation of islands. For high Ge content, the strain build-up after a few layers of layer-by-layer growth leads to strain relaxation by transitioning into island growth. This morphology is characteristic of the well-known Stranski–Krastanov (S–K) growth mode. The sample grown at 600 °C with 80 atom % Ge, which is the point where the transition from F–M to S–K growth mode takes place, is the exact point where defects start to appear, while all the samples below that are defect-free. Moreover, for the growths at 700 °C, when the Ge content is above 90 atom % the SiGe shell is characterized in most cases by island growth only, therefore being dominated by the Volmer–Weber (V–W) growth mode (Figure 3a,d). We note here that the islands (Figure 3c,d) do not seem to exhibit the typical pyramid or dome shape observed in heterostructures with the cubic crystal structure. Because the shape of the island structures formed during S–K and V–W growth depends on the surface energies, one would not expect that the same shapes would appear for the hexagonal crystal structure or for growth on a NW sidewall. On the other hand, we observe that for the growths carried out at 600 °C, the layer-by-layer growth continues up to a Ge content of 80 atom % (Figure 3a,b). This difference in morphology can be understood in terms of the combination of strain and different diffusion lengths of the adatoms for the different growth temperatures, which has been elaborated for metastable layers of cubic SiGe.[34] In particular, strain increases with the Ge content in the shell and at high temperatures the adatom diffusion length is longer. Thus, adatoms can diffuse over longer distances to relieve strain by forming islands. On the other hand, at lower temperatures the adatom diffusion length is shorter, thus the adatom diffusivity is too short to form islands

DOI: 10.1021/acs.nanolett.6b03488
Nano Lett. 2017, 17, 85–90

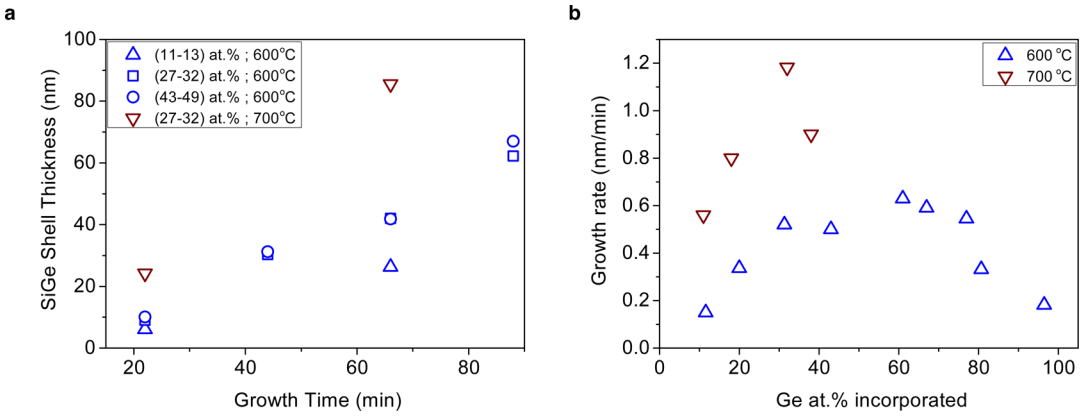

Figure 4. SiGe shell growth kinetics. (a) SiGe shell thickness as a function of growth time for various regions of Ge content, where a linear trend is observed. For the SiGe shells grown at 600 °C at a Ge content in the range of 27−33 atom % and 43−49 atom % the thickness is the same. (b) SiGe shell growth rate as a function of the Ge content of the shell. The growth rate was defined only for F−M growth so all the points in the 600 °C curve represent smooth layer growth. On the other hand, the 700 °C curve exhibits the initial increase but the subsequent decrease is quickly cut off due to the onset of S−K growth.

in the time frame available for growth. As a result, a continuous metastable layer with increasing strain is grown. In summary, from Figure 3 we observe that at the growth temperature of 600 °C not only is the Ge incorporation more efficient but also that layer-by-layer defect-free growth continues up to higher Ge contents, well above the expected direct band gap transition stoichiometry of about $Si_{0.35}Ge_{0.65}$.

The growth kinetics have been studied in more detail and especially the growth rate as a function of time and temperature. The linear dependence of the SiGe thickness with respect to the growth time indicates that the growth rate is roughly constant (Figure 4a). This indicates that the growth rate limiting step is determined by surface kinetics rather than by, for example, volume diffusion. The growth rate depends however on the Ge content. For the growths performed at 600 °C, the shell thickness at 22 min of growth is approximately independent of the Ge content. For longer growth times, the growth rates start to differ; in particular the growth rate for the samples with a Ge content in the range of 11−13 atom % is markedly smaller than for the ones with a Ge content in the range of 27−33 atom % and 43−49 atom % (for which instead the rate is almost the same). This is indicated by a smaller slope for the 11−13 atom % Ge samples, and hence results in a thinner shell, for reasons that we discuss below. For the growths at 700 °C, the thickness doubles for the region of 27−33 atom % Ge relative to the same atom % Ge region at 600 °C.

In addition, the study of the growth rate was performed with a series of samples grown for the whole range of SiGe stoichiometries and for the two different temperatures of 600 and 700 °C. In Figure 4b, we present the growth rate as a function of the Ge content for the two deposition temperatures of the SiGe shell. In terms of the Ge content, two well-differentiated regimes can be observed. First of all, a regime of low Ge content, characterized by a marked increase of the growth rate as the Ge content is increased. In this regime, strain does not influence the growth dynamics and instead the increase in growth rate can be attributed to an increase in hydrogen desorption from the growth surface due to Ge.[26,35−37] Indeed, Ge acts to lower the activation energy of hydrogen desorption, thus freeing-up more surface sites for Si and Ge growth species. This results in an increase in the growth rate with increasing Ge content. The second regime is found in the region with a high Ge content, characterized by a decrease of the growth rate as a function of Ge content. Two different reasons have been proposed to explain this behavior; either high strain[38−40] and/or decreased reactive hydride adsorption.[37] In the first case, strain starts to play the dominant role, and the decrease in the growth rate that takes place is attributed to strain accumulation due to the very high Ge content. Note that as the lattice constant is increased, so is the diffusion energy barrier, and this makes diffusion more difficult. In turn, less diffusion implies a lower growth rate. The second reason for the decreasing growth rate at high Ge content is a decreased reactive hydride adsorption. This has been explained by a lower adsorption coefficient of the precursors, resulting in a lower growth rate. The competition between these different effects is clearly seen in Figure 4b and is in agreement with previous studies.[37−40] While the dependence of the growth rate with the Ge content of the shell shows the same trend for the two temperatures studies, 600 and 700 °C, the quantitative behavior is different. In the case of the growth at high temperature (700 °C), we find that the peak growth rate is higher, and reached for a smaller Ge content than for the growth at low temperatures (600 °C). This behavior can be understood in terms of adsorption and desorption, by a similar mechanism as that discussed above. Indeed, for higher temperatures, besides the decomposition of the precursors both the adatom diffusion and the hydrogen desorption increase, explaining the markedly higher peak growth rates for the shells grown at 700 °C. Furthermore, the 700 °C curve is cut off relatively quickly due to the onset of S−K growth. In essence, Figure 4b further solidifies the claim that for the growth at 600 °C, layer-by-layer defect-free growth continues up to higher Ge contents, above $Si_{0.35}Ge_{0.65}$ where the direct band gap transition is expected to occur.

In conclusion, in this work we have presented the growth of single-crystalline defect-free SiGe with the hexagonal diamond crystal structure. We have reported how the growth temperature can lead to striking differences in the resulting SiGe layer morphology: SiGe layers grown at lower temperatures exhibit uniform layer-by-layer F−M growth, while at higher temperatures and for the same Ge content, island-based S−K growth dominates. The maximum stoichiometry achieved for defect-free smooth layer thin film growth was at 77 atom % Ge, significantly above the predicted direct band gap transition at

DOI: 10.1021/acs.nanolett.6b03488
Nano Lett. 2017, 17, 85−90

65 atom % Ge. Moreover, we observe that layer growth continues to this high value significantly more at the growth temperature of 600 °C. Our results pave the way for the utilization of hexagonal SiGe in optoelectronic applications and in this respect additional studies should be performed for the detailed characterization of the optical properties of this new material.

EXPERIMENTAL METHODS

Nanowire Growth. The GaP/Si/SiGe core/multishell NWs were developed in a low-pressure (50 mbar) Aixtron Close Coupled Showerhead (CCS) MOVPE reactor. The growth of the defect-free GaP/Si core/shell NWs with the hexagonal diamond crystal structure has been described in our previous study.[5] In this case though, the Si shell thickness was kept to a minimum of 10−12 nm. This could potentially act as sacrificial buffer layer to trap any P or Ga species from the GaP core from diffusing into the SiGe shell.

Directly after the growth of the Si shell and in the same growth run, the SiGe shell was grown. This was done by switching off the Si_2H_6 precursor gas and gradually lowering the temperature of the MOVPE growth chamber to either 600 or 700 °C. Once the aimed temperature was reached and stabilized, Si_2H_6 and GeH_4 were introduced to the chamber and their flows were adjusted to suit the desired stoichiometry. Si_2H_6 molar flow was modified from 2.87×10^{-7} at the low end to 1.00×10^{-4} at the high end, whereas GeH_4 was modified from 3.66×10^{-6} at the low end to 3.33×10^{-4} at the high end in order to achieve the desired ratio. Hydrogen (H_2) was used as a carrier gas for the precursors and the total flow into the rector was 8.2 L/min. At the end of the SiGe shell growth, the precursor flows were terminated, the heating elements were switched off and the chamber was allowed to cool down to room temperature.

Transmission Electron Microscopy. For the TEM studies, two different sample preparation methods were used. In the standard axial analysis, NWs were mechanically transferred to a holey carbon TEM grid. Concerning the cross-section TEM studies, NWs were prepared using FIB. In both cases, HRTEM and STEM analyses were conducted using a JEM ARM200F aberration-corrected TEM operated at 200 kV. For the chemical analysis, EDX measurements were carried out using the same microscope equipped with a 100 mm^2 EDX silicon drift detector.

TEM Lamellae. TEM lamellae were prepared in a FEI Nova Nanolab 600i Dualbeam system. For this, the NWs were initially transferred with the aid of a nanomanipulator from the growth substrate to a piece of Si and then arranged to lie parallel to each other. These NWs were covered with electron- and ion-beam induced metal deposition to protect them during the procedure. The lamella was cut out by milling with 30 kV Ga ions and thinned down with subsequent steps of 30, 16, and 5 kV ion milling in order to minimize the Ga-induced damage in the regions imaged with TEM.

AUTHOR INFORMATION

Corresponding Author

*E-mail: e.p.a.m.bakkers@tue.nl.

ORCID

Sebastian Koelling: 0000-0002-6606-9110

Erik P. A. M. Bakkers: 0000-0002-8264-6862

Author Contributions

H.I.T.H conceived the idea and grew the NWs; S.C.B. and M.A.V. performed the TEM analysis of the NWs; H.I.T.H performed the growth rate, kinetics, and growth mode analysis; H.I.T.H, S.C.B., M.A.V., and E.P.A.M.B contributed to the interpretation; S.K. prepared the lamellae for TEM studies; E.P.A.M.B supervised the project. H.I.T.H. and S.C.B. contributed equally to the manuscript.

Notes

The authors declare no competing financial interest.

ACKNOWLEDGMENTS

We would like to thank R. op het Veld for NW transfer for FIB milling, P. J. van Veldhoven for technical support at the MOVPE reactor, A. Cavalli, L. Gagliano, and M. Y. Swinkels for nanoimprint preparation, and A. Li for fruitful discussions. This work was supported by the Dutch Organization for Scientific Research (NWO-VICI 700.10.441), and the European Research Council (ERC CoG HELENA). Solliance is acknowledged for funding the TEM facility.

REFERENCES

(1) Iyer, S. S.; Xie, Y. H. Light Emission from Silicon. *Science* **1993**, *260* (5104), 40−46.

(2) Raffy, C.; Furthmüller, J.; Bechstedt, F. Properties of hexagonal polytypes of group-IV elements from first-principles calculations. *Phys. Rev. B: Condens. Matter Mater. Phys.* **2002**, *66* (7), 075201.

(3) Joannopoulos, J. D.; Cohen, M. L. Electronic Properties of Complex Crystalline and Amorphous Phases of Ge and Si. I. Density of States and Band Structures. *Phys. Rev. B* **1973**, *7* (6), 2644−2657.

(4) De, A.; Pryor, C. E. Electronic structure and optical properties of Si, Ge and diamond in the lonsdaleite phase. *J. Phys.: Condens. Matter* **2014**, *26* (4), 045801.

(5) Hauge, H. I. T.; Verheijen, M. A.; Conesa-Boj, S.; Etzelstorfer, T.; Watzinger, M.; Kriegner, D.; Zardo, I.; Fasolato, C.; Capitani, F.; Postorino, P.; et al. Hexagonal Silicon Realized. *Nano Lett.* **2015**, *15* (9), 5855−5860.

(6) Qiu, Y.; Bender, H.; Richard, O.; Kim, M.-S.; Van Besien, E.; Vos, I.; de Potter de ten Broeck, M.; Mocuta, D.; Vandervorst, W. Epitaxial diamond-hexagonal silicon nano-ribbon growth on (001) silicon. *Sci. Rep.* **2015**, *5*, 12692.

(7) Wentorf, R. H.; Kasper, J. S. Two New Forms of Silicon. *Science* **1963**, *139* (3552), 338−339.

(8) Jennings, H. M.; Richman, M. H. A Hexagonal (Wurtzite) Form of Silicon. *Science* **1976**, *193* (4259), 1242−1243.

(9) Fontcuberta i Morral, A.; Arbiol, J.; Prades, J. D.; Cirera, A.; Morante, J. R. Synthesis of Silicon Nanowires with Wurtzite Crystalline Structure by Using Standard Chemical Vapor Deposition. *Adv. Mater.* **2007**, *19* (10), 1347−1351.

(10) Fabbri, F.; Rotunno, E.; Lazzarini, L.; Cavalcoli, D.; Castaldini, A.; Fukata, N.; Sato, K.; Salviati, G.; Cavallini, A. Preparing the way for doping wurtzite silicon nanowires while retaining the phase. *Nano Lett.* **2013**, *13* (12), 5900−5906.

(11) Algra, R. E.; Hocevar, M.; Verheijen, M. A.; Zardo, I.; Immink, G. G. W.; van Enckevort, W. J. P.; Abstreiter, G.; Kouwenhoven, L. P.; Vlieg, E.; Bakkers, E. P. a M. Crystal Structure Transfer in Core/Shell Nanowires. *Nano Lett.* **2011**, *11* (4), 1690−1694.

(12) Lopez, F. J.; Hemesath, E. R.; Lauhon, L. J. Ordered Stacking Fault Arrays in Silicon Nanowires. *Nano Lett.* **2009**, *9* (7), 2774−2779.

(13) Bandet, J.; Despax, B.; Caumont, M. Vibrational and electronic properties of stabilized wurtzite-like silicon. *J. Phys. D: Appl. Phys.* **2002**, *35* (3), 234−239.

(14) Liu, X.; Wang, D. Kinetically-induced hexagonality in chemically grown silicon nanowires. *Nano Res.* **2009**, *2* (7), 575−582.

DOI: 10.1021/acs.nanolett.6b03488
Nano Lett. 2017, 17, 85−90

(15) Pirouz, P.; Chaim, R.; Dahmen, U.; Westmacott, K. H. The martensitic transformation in silicon—I experimental observations. *Acta Metall. Mater.* **1990**, *38* (2), 313−322.
(16) Li, F.; Nellist, P. D.; Lang, C.; Cockayne, D. J. H. Imaging and analysis of axial heterostructured silicon nanowires. *J. Phys. Conf. Ser.* **2010**, *241* (1), 012088.
(17) Arbiol, J.; Kalache, B.; Roca i Cabarrocas, P.; Morante, J. R.; Fontcuberta i Morral, A. Influence of Cu as a catalyst on the properties of silicon nanowires synthesized by the vapour−solid−solid mechanism. *Nanotechnology* **2007**, *18* (30), 305606.
(18) Arbiol, J.; Fontcuberta i Morral, A.; Estradé, S.; Peiró, F.; Kalache, B.; Roca i Cabarrocas, P.; Morante, J. R. Influence of the (111) twinning on the formation of diamond cubic/diamond hexagonal heterostructures in Cu-catalyzed Si nanowires. *J. Appl. Phys.* **2008**, *104*, 064312.
(19) Vincent, L.; Patriarche, G.; Hallais, G.; Renard, C.; Gardès, C.; Troadec, D.; Bouchier, D. Novel Heterostructured Ge Nanowires Based on Polytype Transformation. *Nano Lett.* **2014**, *14* (8), 4828−4836.
(20) Xiao, S.-Q.; Pirouz, P. On diamond-hexagonal germanium. *J. Mater. Res.* **1992**, *7* (06), 1406−1412.
(21) Persson, C.; Janzén, E. Electronic band structure in hexagonal close-packed Si polytypes. *J. Phys.: Condens. Matter* **1998**, *10* (47), 10549−10555.
(22) Stroud, D.; Ehrenreich, H. Band Structure of SiGe: Coherent-Potential Approximation. *Phys. Rev. B* **1970**, *2* (8), 3197−3209.
(23) Fischetti, M. V.; Laux, S. E. Band structure, deformation potentials, and carrier mobility in strained Si, Ge, and SiGe alloys. *J. Appl. Phys.* **1996**, *80* (4), 2234.
(24) Iori, F.; Ossicini, S.; Rurali, R. Structural and electronic properties of $Si_{1-x}Ge_x$ alloy nanowires. *J. Appl. Phys.* **2014**, *116*, 154301.
(25) Amato, M.; Palummo, M.; Ossicini, S. Band structure analysis in SiGe nanowires. *Mater. Sci. Eng., B* **2012**, *177* (10), 705−711.
(26) Varahramyan, K. M.; Ferrer, D.; Tutuc, E.; Banerjee, S. K. Band engineered epitaxial Ge−Si_xGe_{1-x} core-shell nanowire heterostructures. *Appl. Phys. Lett.* **2009**, *95*, 033101.
(27) Goldthorpe, I. a.; Marshall, A. F.; McIntyre, P. C. Inhibiting Strain-Induced Surface Roughening: Dislocation-Free Ge/Si and Ge/SiGe Core−Shell Nanowires. *Nano Lett.* **2009**, *9* (11), 3715−3719.
(28) Goldthorpe, I. A.; Marshall, A. F.; McIntyre, P. C. Synthesis and Strain Relaxation of Ge-Core/Si-Shell Nanowire Arrays. *Nano Lett.* **2008**, *8* (11), 4081−4086.
(29) Conesa-Boj, S.; Hauge, H. I. T.; Verheijen, M. A.; Assali, S.; Li, A.; Bakkers, E. P. A. M.; Fontcuberta i Morral, A. Cracking the Si Shell Growth in Hexagonal GaP-Si Core−Shell Nanowires. *Nano Lett.* **2015**, *15* (5), 2974−2979.
(30) Arkles, B. Silicon Compounds, Silanes. In *Kirk-Othmer Encyclopedia of Chemical Technology*; John Wiley & Sons, Inc.: Hoboken, NJ, 2000.
(31) Hogness, T. R.; Johnson, W. C. The catalytic decomposition of germane. *J. Am. Chem. Soc.* **1932**, *54* (9), 3583−3592.
(32) Tamaru, K.; Boudart, M.; Taylor, H. The Thermal Decomposition of Germane. I. Kinetics. *J. Phys. Chem.* **1955**, *59* (9), 801−805.
(33) Paul, D. J. Si/SiGe heterostructures: from material and physics to devices and circuits. *Semicond. Sci. Technol.* **2004**, *19* (10), R75−R108.
(34) Sunamura, H.; Shiraki, Y.; Fukatsu, S. Growth mode transition and photoluminescence properties of $Si_{1-x}Ge_x$/Si quantum well structures with high Ge composition. *Appl. Phys. Lett.* **1995**, *66* (8), 953.
(35) Hirose, F.; Sakamoto, H. Desorption rate of surface hydrogen in SiGe gas-source molecular beam epitaxy using Si_2H_6 and GeH_4. *J. Vac. Sci. Technol., A* **1998**, *16* (5), 2974.
(36) Vizoso, J.; Martín, F.; Suñé, J.; Nafría, M. Hydrogen desorption in SiGe films: A diffusion limited process. *Appl. Phys. Lett.* **1997**, *70* (24), 3287.
(37) Gu, S.; Zheng, Y.; Zhang, R.; Wang, R.; Zhong, P. Ge composition and temperature dependence of the deposition of SiGe layers. *J. Appl. Phys.* **1994**, *75* (10), 5382.
(38) Cherepanov, V.; Voigtländer, B. Influence of strain on diffusion at Ge(111) surfaces. *Appl. Phys. Lett.* **2002**, *81* (25), 4745.
(39) Hoshino, T.; Hata, M.; Tsuda, M. Migration of Si adatom on strained Si(111) surfaces. *Surf. Sci.* **2001**, *481* (1−3), 205−214.
(40) Ratsch, C.; Seitsonen, A. P.; Scheffler, M. Strain dependence of surface diffusion: Ag on Ag(111) and Pt(111). *Phys. Rev. B: Condens. Matter Mater. Phys.* **1997**, *55* (11), 6750−6753.

DOI: 10.1021/acs.nanolett.6b03488
Nano Lett. 2017, 17, 85−90